ACS OMEGA

http://pubs.acs.org/journal/acsodf

Article

Natural N-Doped Carbon Quantum Dots Derived from Straw and Adhered onto TiO_2 Nanospheres for Enhancing the Removal of Antibiotics and Resistance Genes

Bei Yang, Yingliang Yu, Hao Liu, Linzhang Yang, Zulin Hua, Yanfang Feng, and Lihong Xue*

Cite This: *ACS Omega* 2023, 8, 718−725

Read Online

ACCESS | Metrics & More | Article Recommendations | Supporting Information

ABSTRACT: Antibiotics and antibiotic resistance genes (ARGs) are emerging environmental contaminants. TiO_2 photocatalytic degradation has been proved an important removal technique, but its photocatalytic ability needs be improved. In our work, natural N-doped carbon quantum dots (N-SCQDs) were extracted from hydrothermal carbonization waste liquid of straw and were attached onto TiO_2 nanospheres for remediating antibiotics [sulfadiazine (SA)] and ARGs (*sul*1, *sul*2, and *intl*1). The maximum SA reduction rates were close to 100%, and the ARG reduction rates were 52.91−83.52%/lg10 (*sul*1), 32.10−68.23%/lg10 (*sul*2), and 46.29−76.55%/lg10 (*inlt*1). The temperature of the straw derivatives would influence their photoelectric properties. N-SCQDs@TiO_2 expands the application range of a novel potential high-efficiency degradation catalyst and offers a new way of hydrothermal carbonization waste liquid of agricultural waste.

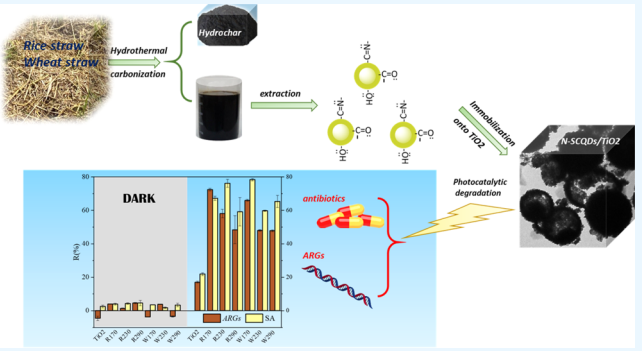

1. INTRODUCTION

Antibiotics are widely used in human medicine and in livestock animals for prophylactic, therapeutic, and growth-promoting purposes. However, their excessive use can lead to the development and spread of antibiotic resistance genes (ARGs) in the environment. Consequently, antibiotics and ARGs are considered emerging environmental contaminants and have already been detected in diverse environmental compartments.[1,2] Among the various remediation methods for ARGs, advanced chemical oxidation processes have attracted scientific interest because of the generation of reactive oxygen species (ROS), which are promising alternatives for degrading antibiotics in wastewater.[3−6]

CQDs are typical quasi-spherical nanoparticles with amorphous to nanocrystalline cores. Because of the fluorescence upconversion effect, CQDs can expand the light absorption range; they can also promote the separation of photogenerated electrons and holes because of their excellent charge transfer ability.[7−11] CQDs are synthesized through various techniques, including ultrasonic methods, hydrothermal treatment, microwave-assisted synthesis, strongly acidic and electrochemical oxidation, and glycerol pyrolysis.[12−16]

Compared with pure TiO_2, TiO_2 combined with the produced CQDs had more excellent photocatalytic degradation ability.[17] Through a hydrothermal treatment, Wang et al. loaded CQDs on the surface of TiO_2 to form a CQDs/TiO_2 composite and found that the degradation rates of 5% CQDs/TiO_2 reached 81 and 92% for tetracycline and rhodamine B, respectively. Zeng et al. described the photocatalytic ozonation degradation of ciprofloxacin by a TiO_2/CQDs photocatalyst prepared by the hydrothermal−calcination method coupled. The photocatalytic efficiency was 91.1% for an irradiation time of 30 min. Liu et al. reported the photocatalytic degradation of tetracycline using a combination of oxygen-rich TiO_2 nanosheets and CQDs (CQD-OTNs), in which the CQD-OTNs could increase the degradation ratio of tetracycline to 94.1% with 120 min visible light irradiation.[18−20] However, most studies of CQDs/TiO_2 focused on the removal of traditional antibiotics or organic substances and neglected the emerging pollutant, especially for ARGs. According to the photoelectric property of CQDs/TiO_2, we can infer that it may have potential to remove ARGs and is worthy of further excavation and utilization.

As well known, CQDs can be synthesized from a wide source of raw materials and have low costs.[21] Straw is a typical agricultural waste that has attracted the attention of researchers. In our previous study, carbonization of straw was for preparation of biochar,[22−24] but the byproduct of the

Received: September 15, 2022
Accepted: November 28, 2022
Published: December 27, 2022

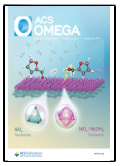

carbonization process was ignored, such as hydrothermal carbonization waste liquid, which is an important resource of CQDs. What is more, crops absorb N fertilizer and retain part of N in straw, and straw possesses the neutral advantage of formatting N-doping. Therefore, hydrothermal byproducts of straw can be fully exploited.

In this study, CQDs were first extracted from hydrothermal liquid [straw carbon quantum dots (N-SCQDs)]. After the straw was hydrothermally decomposed and N-SCQDs were synthesized and separated by centrifugation, hydrothermal biochar was produced as a lower sediment. To our knowledge, this work was the first to use straw as a CQD precursor and to experimentally discuss the effect of extraction hydrothermal temperature on the antibiotic and ARG removal ability of the resultant CQDs.

2. RESULTS AND DISCUSSION

A series of photodegradation experiments were performed for testing removal ability. In Figure 1, after 120 min under dark

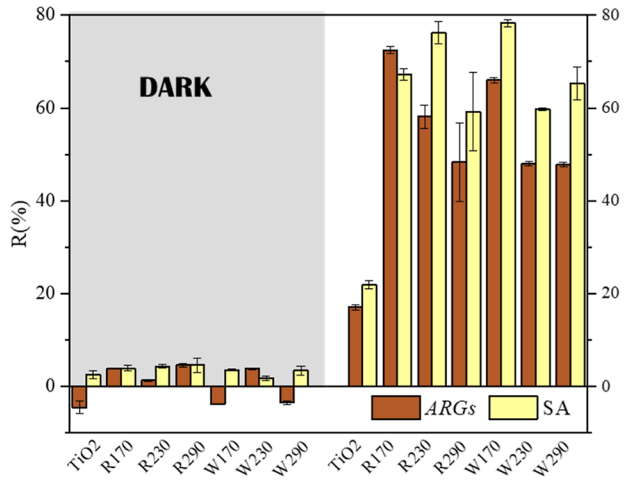

Figure 1. Removal ability of N-SCQDs@TiO_2 under dark or UV light conditions.

conditions, the sulfadiazine (SA) concentration decreased to 10%; the total quantity of ARGs decreased to 3% and even had negative growth. The removal ability of N-SCQDs@TiO_2 in the dark was poor, indicating that N-SCQDs@TiO_2 was not a good SA and ARGs adsorbent. SA has two ionization constants in aqueous solution: pK_{a1} = 1.57 and pK_{a2} = 6.48.[25] Therefore, when pH = 1.57−6.48, SA exists in the form of a neutral molecule, which disables the electrostatic adsorption ability of N-SCQDs@TiO_2. Under UV light, the SA concentration decreased to 21.86−78.31%, and the total quantity of ARGs decreased to 17.10−72.39%. These results indicated that light was the key factor driving the removal effect, and removal depended on photodegradation. The removal ability of all N-SCQDs@TiO_2 was better than that of pure TiO_2 by 2−4 times. The results proved that N-SCQDs could assist TiO_2 in degradation.

With an increase in the added amount of N-SCQDs@TiO_2, the removal efficiency increased gradually (Figure 2a) because the increased adsorbent provided more active sites. However, when the added amount was more than 1 g/L, the removal efficiency stopped increasing, implying that 1 g/L was the optimal amount to achieve the best effect. The removal efficiency decreased with the increasing initial concentration because the number of available active sites on the adsorbent decreased as the concentration increased (Figure 2b). Regardless of pollution concentration, all the removal rates of SA exceeded 70%, and the highest was 99.03% (SA concentration = 10 mg/L). Thus, SCQDs/TiO_2 could effectively remove SA, suggesting that it has a wide range of applications and is a potentially efficient processing material. The dynamic SA degradation catalyzed by different SCQDs/TiO_2 materials at different initial SA concentrations was displayed in the supplement.

ARGs play an important role in horizontal transfer mechanisms, which are considered macromolecular organisms. Organic ARGs can be completely destroyed by photocatalytic oxidation, whose advantages include the requirement of mild reaction conditions and strong oxidation ability. Therefore, in the present study,[3−5,26] the relevant ARGs (*sul*1, *sul*2, and *intl*1) were investigated before and after degradation. The removal rates of ARGs were in the range of 52.91−83.52%/lg10 (*sul*1, Figure 2c), 32.10−68.23%/lg10 (*sul*2, Figure 2d), and 46.29−76.55%/lg10 (*inlt*1, Figure 2e). ARGs were removed by N-SCQDs/TiO_2 materials. The quantity of added N-SCQDs/TiO_2 materials did not evidently affect ARG removal rates. For different types of N-SCQDs/TiO_2 obtained under different conditions, the ARGs removal rate was reduced with the increase in hydrothermal temperature during material production. As explained previously, this reduction occurred because oxidants such as ROS produced by indirect photolysis preferentially reacted with guanine bases in the DNA. Indirectly, photocatalysis-produced ROS was mainly responsible for ARG degradation.[26,27]

A series of nearly spherical N-SCQDs with a uniform size by typical high-resolution transmission electron microscopy (HR-TEM) images (Figure 3a) were successfully anchored onto the surface of the TiO_2 nanospheres. N-SCQDs obtained at 170, 230, and 290 °C had average diameters of ∼20, ∼10, and ∼2 nm, respectively. Clearly, when the hydrothermal temperature increased, the average particle size decreased. The characteristic peaks were observed at 2θ = 25.26, 37.89, and 47.99°, corresponding to the diffraction peaks of (101), (004), and (200) crystal planes of the TiO_2 anatase phase, respectively, indicating the existence of this phase in the composite product (Figure 3b). As shown in Figure 3c, no obvious displacement or peak type changes in each diffraction peak occurred, demonstrating that changes in preparation temperature and biomass raw materials did not affect the crystal form of the N-SCQDs@TiO_2 composite. The wide peaks centered at 3225−3420 cm^{-1} in the infrared spectrum were caused by the stretching vibration of C−OH, indicating that N-SCQDs@TiO_2 has a hydrophilic nature. The peaks at 2880−2985 and 1420−1450 cm^{-1} originated from the stretching vibration of C−H. The peaks appearing at approximately 1600 cm^{-1} were assigned to the asymmetric and symmetric stretching vibrations of carboxyl anions, which are consistent with the infrared spectrum of the CQDs. The peaks observed at 1114 cm^{-1} originated from the C−N moiety, whereas those at 484 and 465 cm^{-1} were the characteristic vibrations of the Ti−O bond.

The proportions of the areas of the peak characteristics of C(1s), O(1s), and Ti(2p) are listed in Table 1. When the hydrothermal temperature increased, the C content first increased and then decreased, whereas the O and Ti contents initially decreased and subsequently decreased. The peaks in the full-scan spectrum (Figure 4a) indicated that the TiO_2

https://doi.org/10.1021/acsomega.2c05979
ACS Omega 2023, 8, 718−725

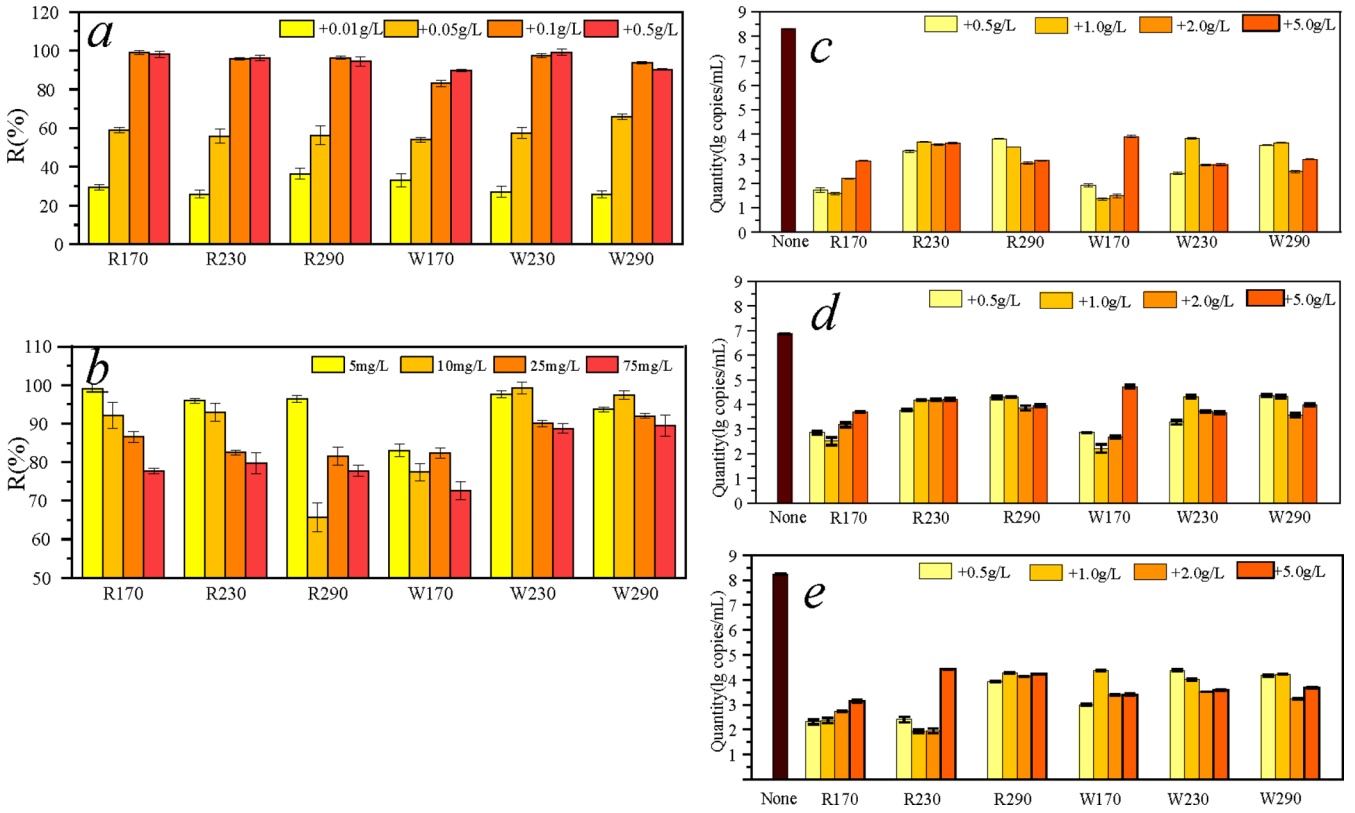

Figure 2. (a) Removal effect of SA by different addition amounts; (b) removal effect of SA by different initial concentrations; (c) removal effect of *sul*1 by different addition amounts; (d) removal effect of *sul*2 by different addition amounts, and (e) removal effect of *inlt*1 by different addition amounts.

nanoparticles were successfully packaged by N-SCQDs, and the influence of hydrothermal temperature was irregular. Weak N peaks corresponding to different forms of nitrogen doping could be observed. In particular, the peak at 400.6 eV was characteristic of nitrogen atoms replacing the carbon atom of a pyridine-shaped carbocyclic ring, and the peak at 399.2 eV was characteristic of nitrogen atoms replacing a quaternary-shaped carbocyclic ring. Regarding the C(1s) area, a few main peaks existed: C−C (284.7 eV), C−O (286.4 eV), and C−N (288.1 eV). The proportions of the area of C−N peaks were 8.41% (R170), 0.86% (R230), 1.44% (R290), 1.23% (W170), 2.58% (W230), and 4.75% (W290). Nitrogen doping is effective in changing the optical and electrical properties of bulk semiconductor materials. N-Doped CQDs have a small band gap and absorb light in the visible region.[28−30] The existence of N implied the presence of natural biomass precursors with various constituent elements; consequently, such precursors present the advantage of natural nitrogen doping over synthetic precursors.[31−33] Based on chemical structure analysis, the hypothesis was that N-SCQDs may improve the photodegradation ability of TiO_2.

The fluorescence emission spectra of N-SCQDs@TiO_2 were studied at full excitation wavelengths (Figure 4b). All the N-SCQDs@TiO_2 composites were studied, giving rise to similar fluorescence light curves. The maximum fluorescence intensity was obtained at an excitation wavelength of 541 nm possibly because of the existence of various electron transition levels in N-SCQDs@TiO_2 due to different surface states and wide particle size distributions. The fluorescence intensity at 514 nm and the hydrothermal extraction temperature exhibited a good linear relationship. The fluorescence spectrum was also used to analyze the separation of photogenerated electrons and holes in the semiconductor photocatalysts. For a low fluorescence intensity, low energy is generated by the recombination of photogenerated electrons and holes in a material. In this case, the composite exhibits an improved efficiency in separating photogenerated electrons and holes and an enhanced photocatalytic performance. As shown in Figure 4b, the fluorescence intensity of TiO_2 was the highest among the values obtained in this study.

The fluorescence intensity of all the N-SCQDs@TiO_2 composites (Figure 4b) was lower than those of other composites, showing that their carrier separation efficiency and photocatalytic activity were higher than those of other composites. Notably, the fluorescence intensity of the wheat straw-derived N-SCQDs@TiO_2 samples was lower than that of the rice straw-derived samples. Therefore, the degradation ability of the N-SCQDs@TiO_2 derived from wheat straw was higher than that of the N-SCQDs@TiO_2 derived from rice straw. This phenomenon can be observed in materials with paramagnetic properties through the analysis of the electron spin resonance spectra of paramagnetic substances; thus, unpaired electron states in relevant substances can be determined. Electrochemical impedance spectroscopy (EIS) was used to analyze the charge transfer behavior at the photocatalyst interface (Figure S2). The EIS results are consistent with the photoluminescence (PL) results.

Electron paramagnetic resonance (EPR) analysis was conducted to determine if different N-SCQDs@TiO_2 had unpaired electrons (Figure 4c). The prominent signal observed at g = 2.005 was assigned to oxygen vacancies, and a pair of weak signals detected at g = 1.9832 and 1.9567 were assigned

https://doi.org/10.1021/acsomega.2c05979
ACS Omega 2023, 8, 718−725

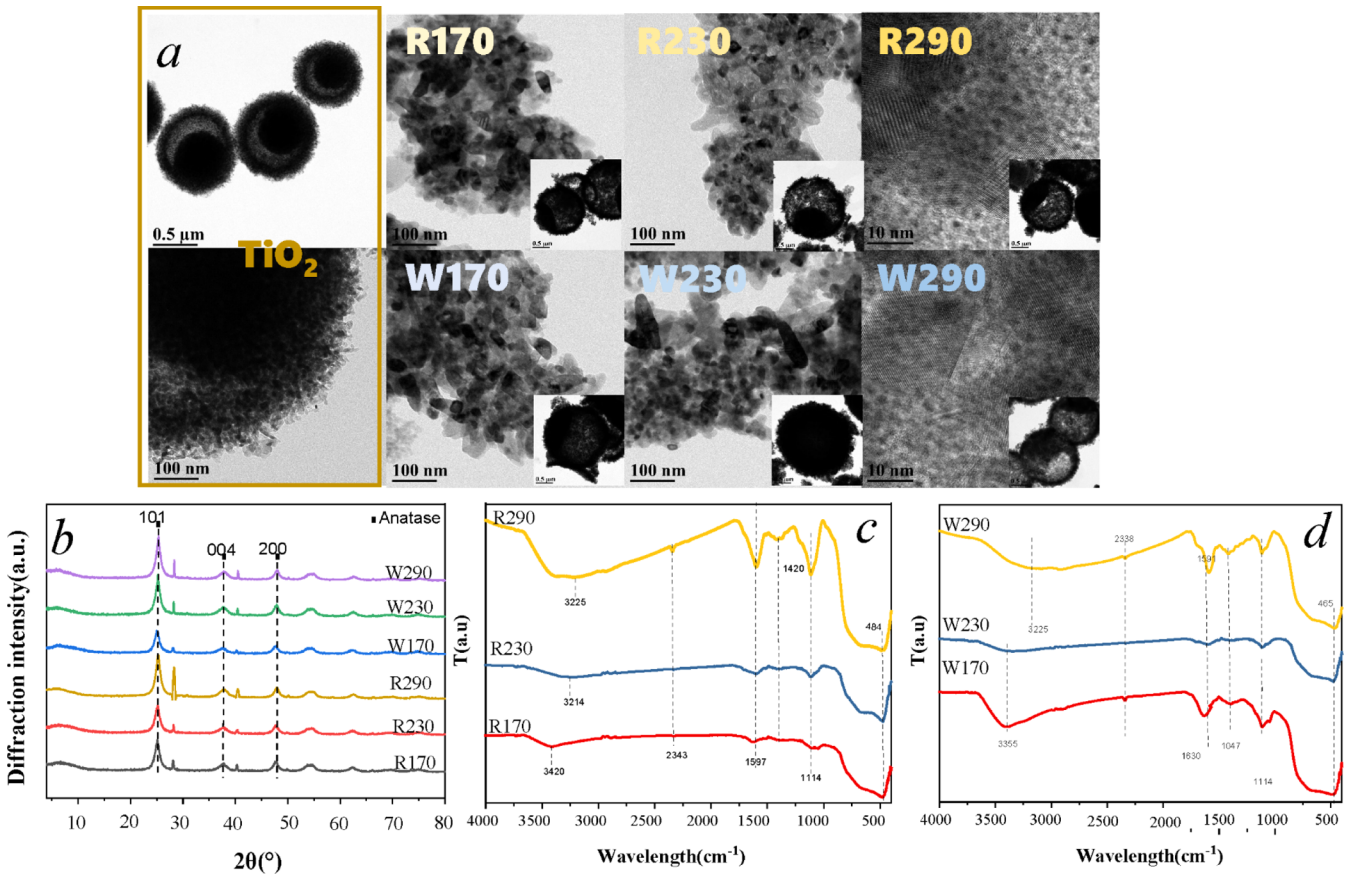

Figure 3. (a) HR-TEM images of N-SCQDs@TiO_2; (b) X-ray powder diffraction spectrum of N-SCQDs@TiO_2; and (c,d) Fourier transform infrared spectrum of N-SCQDs@TiO_2.

Table 1. Proportion of the Area of C(1s), O(1s), and Ti(2p) Peaks

proportion	C(1s) (%)	O(1s) (%)	Ti(2p) (%)
R170	71.12	23.54	5.34
R230	78.65	17.32	4.04
R290	70.99	21.98	7.03
W170	75.08	19.5	5.42
W230	80.71	16.76	2.54
W290	66.77	25.44	7.79

to the Ti^{3+} states. The weak peak located at g = 2.014 corresponded to the capture of O_2 by the Ti^{3+} sites at the surface. Generally, the existing surface Ti^{3+} sites can be easily oxidized by surface-adsorbed O_2 molecules to form $^{\bullet}O^{2-}$. Comparing the surface defect degrees of the different types of N-SCQDs@TiO_2, the highest was observed in W290, whereas the lowest was detected in R170. Moreover, the defect degree increased with the increasing hydrothermal temperature. The defect degree of wheat derivatives was higher than that of rice derivatives, implying that the photocatalytic capacity of wheat derivatives was higher than that of rice derivatives.

By summarizing the results of the degradation experiment and the extensive characterization via X-ray photoelectron spectroscopy (XPS), PL, EIS, and EPR, we found that N-SCQDs derived from straw can improve the photocatalytic capacity of TiO_2 nanospheres. Under light irradiation, when the incident light energy is higher than the difference between the valence band and conduction band energy, electrons in the valence band become excited, and electron transition to the conduction band occurs, accompanied by the generation of electrons (e^-) and holes (H^+). TiO_2-generated electrons are transferred to the N-SCQDs through the interface to achieve an energy level interface balance, thereby prolonging the lifetime of the photogenerated electrons and inhibiting the recombination of electrons and holes. These electrons can oxidize O_2, create superoxide radicals, and generate hydroxyl radicals.[34−37]

3. CONCLUSIONS

The combined N-SCQDs/TiO_2 material could remove SA and its relevant resistance genes (*sul*1, *sul*2, and *inlt*1) from aqueous solutions. The removal degree of SA was close to 100% (0.1 g/L, [SA] = 10 mg/L). N-SCQDs@TiO_2 could effectively remediate sulfonamide pollution over a wide concentration range (5−75 mg/L) and the SA removal was accomplished through degradation. The ARG removal rates by N-SCQDs@TiO_2 were 52.91−83.52%/lg10 (*sul*1), 32.10−68.23%/lg10 (*sul*2), and 46.29−76.55%/lg10 (*inlt*1). Through a series of characterizations, we found that using natural straw for material production provided the advantage of natural nitrogen doping in the resulting N-SCQDs@TiO_2; the type of precursor (wheat or rice) influenced the chemical structure and photoelectric properties of the N-SCQDs@TiO_2: the overall photocatalytic properties of wheat straw derivatives were better than those of rice straw derivatives; the particle size of N-SCQDs decreased with an increase in the preparation temperature; and the preparation temperature of the straw derivatives influenced their photoelectric properties: generally,

https://doi.org/10.1021/acsomega.2c05979
ACS Omega 2023, 8, 718−725

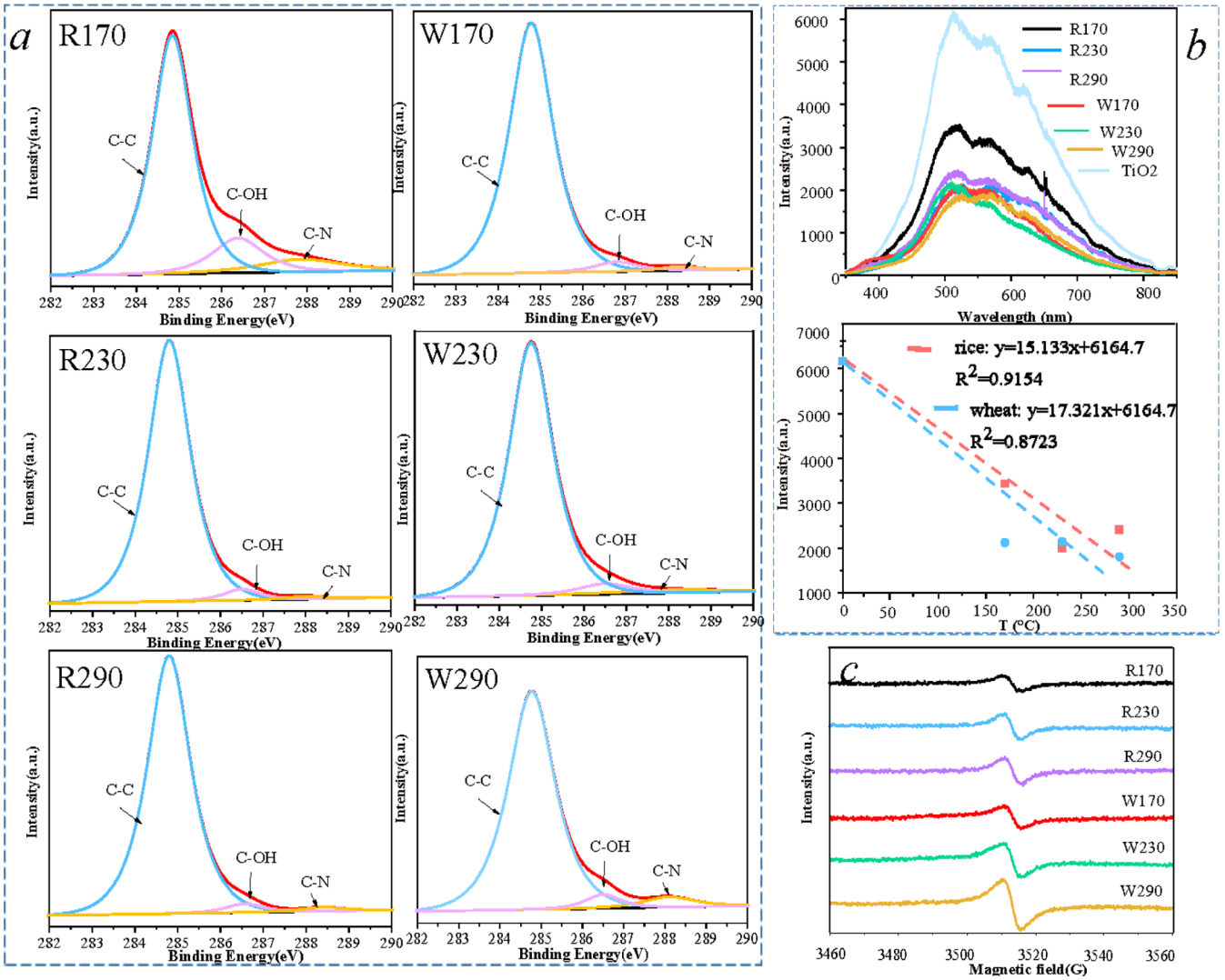

Figure 4. (a) C(1s) X-ray photoelectron spectroscopy of N-SCQDs@TiO_2; (b) PL spectrum for N-SCQDs@TiO_2 and TiO_2; and (c) EPR spectrum of N-SCQDs@TiO_2.

the higher the production temperature, the better the photoelectric properties. The degradation mechanism was attributed to the transfer of electrons to the TiO_2 conduction band, which was promoted by the N-SCQDs due to their strong electron transfer ability. These results not only demonstrate the practicability of N-SCQDs@TiO_2 as a potential high-efficiency degradation catalyst but also confirm the possibility of using straw as a CQD precursor.

4. EXPERIMENTAL SECTION

4.1. Materials. Rice and wheat straw was obtained from the experimental fields of our research group. They were dried to a constant weight and ground (particle size less than ~10 mm). TiO_2 nanoparticles and SA (99.9%), as model pharmaceutical pollutants, were obtained from Sigma-Aldrich, USA. Analytical-grade ethanol, nitric acid, hydrochloric acid, and sodium hydroxide were purchased from Sinopharm Chemical Reagent Co. Ltd. (Shanghai, China). Spectrographic-grade acetonitrile was purchased from Macklin Biochemical Co. Ltd. (China). Deionized water was used to prepare the stock solutions to prevent ion interference. Rural domestic sewage tail water was collected from a village sewage treatment plant in Nanjing.

4.2. Extraction and Immobilization of N-SCQDs. 2 g of straw powder (rice or wheat) was mixed with 50 mL of ultrapure water for 2 h. The mixture was then poured into a high-temperature water reactor for 6 h. The hydrothermal reaction was performed at 170, 230, and 290 °C. After the reaction, the mixture was centrifuged at 1000 rpm for 10 min, yielding a supernatant containing CQDs and a precipitate containing hydrothermal biochar for other purposes. The N-SCQD solutions must be stored at a low temperature and in the dark.

TiO_2 nanoparticles (0.40 g) and N-SCQD solutions (16 mL) were magnetically stirred for 1 h. The mixed solution was poured into a high-temperature hydrothermal reactor, and the reaction was performed at 120 °C for 4 h. Then, the mixture was centrifuged at 1000 rpm for 10 min, and the precipitate was further treated. After being washed, the precipitate was dried in an oven at 60 °C to obtain the product. The nomenclature of the samples is presented in Table 2.

4.3. Experimental Study on the Removal of SA and Its Relevant ARGs. The performance of N-SCQDs@TiO_2 was evaluated in a BL-GHX-V photoreactor.

Dark experiments were conducted to test the adsorption ability of the composites. N-SCQDs@TiO_2 (0.1 g/L) was

https://doi.org/10.1021/acsomega.2c05979
ACS Omega 2023, 8, 718−725

Table 2. Nomenclature of N-SCQDs@ TiO_2

	hydrothermal temperature		
straw	170 °C	230 °C	290 °C
rice	R170	R230	R290
wheat	W170	W230	W290

added to a quartz tube previously filled with aqueous SA suspensions (10 mg/L). Prior to irradiation, the suspensions were magnetically stirred in the dark for 2 h to attain equilibrium adsorption at 25 °C. During the reaction, the samples were regularly withdrawn with a syringe for 1 h and filtered through a 0.22 μm membrane filter to prepare them for SA concentration analysis.

A series of photodegradation experiments were performed. Different N-SCQDs@TiO_2 materials were added to quartz tubes filled with the SA solutions (10 mg/L, 100 mL). Prior to irradiation, the suspensions were magnetically stirred under a 20 W UV lamp irradiating at 265 nm at 25 °C for 8 h. The samples for SA concentration analysis were withdrawn with a syringe at time intervals and filtered through a 0.22 μm membrane filter. The reactions were performed using different amounts of N-SCQDs@TiO_2 (1, 5, 10, and 50 mg).

N-SCQDs@TiO_2 was added to quartz tubes filled with aqueous SA solutions at different concentrations (5−75 mg/L, 1 g/L). Prior to irradiation, the suspensions were magnetically stirred under a 20 W UV lamp at 265 nm at 25 °C for 8 h. The samples were withdrawn at reaction times of 5−480 min and filtered through a 0.22 μm membrane filter for SA concentration analysis.

Different N-SCQDs@TiO_2 types and quantities (25, 50, 100, and 250 mg) were added to quartz tubes filled with rural domestic sewage tailwater (50 mL). Prior to irradiation, the suspensions were magnetically stirred under a 20 W UV lamp at 265 nm or in the dark at 25 °C for 2 h. After irradiation, the aqueous solutions (50 mL) were vacuum-filtered through cellulose acetate membrane filters (0.22 μm) to capture aquatic microorganisms, and the membranes were placed in Lysing Matrix E tubes. A commercial kit (FastDNA Spin Kit for Soil, MP Biomedicals, USA) was used to extract DNA.

The removal rate can be simplified as follows

$$R = \frac{C_0 - C_A}{C_0} \times 100\% \quad (1)$$

where C_0 and C_A are the initial and equilibrium concentrations.

SA concentrations were analyzed via high-performance liquid chromatography (Agilent Technologies 1200 Series, USA) by using a 4.6 mm × 250 mm Athena C18-WP column and a UV detector. The following parameters were set: mobile phase, water: acetonitrile (3:1, V/V); flow rate, 1.0 mL/min; the detection wavelength of the UV detector, 269 nm; column temperature, 30 °C; injection volume, 10 μL; and single injection time, 10 min. The characteristic SA peak appeared at a retention time of 4 min.

The DNA extraction rate was analyzed by performing gel electrophoresis (1.2% agarose concentration) and using an ultra-micro-UV spectrophotometer (NanoDrop 2000, USA). DNA concentrations were calculated based on OD_{260}. The absorption ratio of $OD_{260/280}$ in this study was between 1.8 and 2.0. The extracted DNA samples were stored at −40 °C prior to polymerase chain reaction (PCR) assays. Before the PCR tests, the extracted DNA samples were diluted five times (~5 ng DNA/mL) to reduce interference with the reaction (Table 3).

5. CHARACTERIZATION

The crystalline morphology of the samples was examined by HR-TEM (Tecnai G2 F20, USA). X-ray powder diffraction (XRD) was conducted using an AXS D8 Bruker Advance XRD instrument with Cu Kα1 radiation. The functional groups of the samples were analyzed using Fourier transform infrared spectroscopy (Vertex 70, Germany). XPS (Thermo Fisher Scientific ESCALAB 250Xi, USA) was performed. High-resolution measurements were conducted at a pass energy of 200 eV. XPS Peak 4.0 was used to fit the XPS spectral peaks. The resulting diffractograms were analyzed using MDI Jade 6.0. PL spectra were obtained using a SPEX fluorescence spectrometer (Horika Company, Japan). The voltage was 700 V, a xenon lamp was used as a light source, and the incident and emission light slits were 2.5 nm. EIS were obtained using an electrochemical workstation (Chenhua-chi660, China). Sodium sulfate (7.1 g/L), a standard Ag/AgCl electrode, and a 1 cm × 1 cm platinum plate electrode were used as an electrolyte, reference electrode, and indicator electrode, respectively. The prepared electrode was then used as the working electrode. EPR spectra were recorded using an X-band EMX spectrometer (Bruker, Germany) with a standard rectangular cavity of ER 4102 at room temperature.

■ ASSOCIATED CONTENT

Supporting Information

The Supporting Information is available free of charge at https://pubs.acs.org/doi/10.1021/acsomega.2c05979.

Displayed dynamic SA degradation process; calculated SA degradation kinetics; and EIS analysis data of the N-SCQDs@TiO_2 sample (PDF)

■ AUTHOR INFORMATION

Corresponding Author

Lihong Xue − *Key Laboratory of Food Quality and Safety of Jiangsu Province-State Laboratory Breeding Base, Jiangsu Academy of Agricultural Sciences, Nanjing 210014, China*; Email: njxuelihong@gmail.com

Table 3. Primers and PCR Conditions[38]

target	size (bp)	primer sequences (5′-3′)	[1]annealing temperature (°C)	linearity (R^2)	efficiency (%)
*sul*1	172	FW CACCGGAAACATCGCTGCA	57 (T)	0.99	92
		RV AAGTTCCGCCGCAAGGCT	55 (Q)		
*sul*2	165	FW CTCCGATGGAGGCCGGTAT	60 (T)	0.99	95
		RV GGGAATGCCATCTGCCTTGA	55 (Q)		
*intl*1	190	FW GGCTTCGTGATGCCTGCTT	60 (T)	0.99	97
		RV CATTCCTGGCCGTGGTTCT	57(Q)		

https://doi.org/10.1021/acsomega.2c05979
ACS Omega 2023, 8, 718−725

Authors

Bei Yang − *Key Laboratory of Food Quality and Safety of Jiangsu Province-State Laboratory Breeding Base, Jiangsu Academy of Agricultural Sciences, Nanjing 210014, China;* orcid.org/0000-0003-0929-0078

Yingliang Yu − *Key Laboratory of Food Quality and Safety of Jiangsu Province-State Laboratory Breeding Base, Jiangsu Academy of Agricultural Sciences, Nanjing 210014, China*

Hao Liu − *Key Laboratory of Water Control in Taihu Lake Basin, Ministry of Water Resources, Nanjing Hydraulic Research Institute, Nanjing 210029, China*

Linzhang Yang − *Key Laboratory of Food Quality and Safety of Jiangsu Province-State Laboratory Breeding Base, Jiangsu Academy of Agricultural Sciences, Nanjing 210014, China*

Zulin Hua − *Key Laboratory of Integrated Regulation and Resources Development of Shallow Lakes, Ministry of Education, College of Environment, Hohai University, Nanjing 210098, China*

Yanfang Feng − *Key Laboratory of Food Quality and Safety of Jiangsu Province-State Laboratory Breeding Base, Jiangsu Academy of Agricultural Sciences, Nanjing 210014, China*

Complete contact information is available at: https://pubs.acs.org/10.1021/acsomega.2c05979

Author Contributions

The manuscript was written by B.Y., and all authors have contributed to this manuscript and given approval to the final version of the manuscript.

Notes

The authors declare no competing financial interest.

■ ACKNOWLEDGMENTS

The authors gratefully acknowledge the support provided by National Key Research and Development Program (2021YFD1700805), Jiangsu Provincial Key Research and Development Program (D21YFD17008), and independent research project of Key Lab of Food Quality and Safety of Jiangsu Province-State Laboratory Breeding Base. We also thank Wu Rong and Cao Junlu for assistance in experiment operation.

■ REFERENCES

(1) Xu, T.; Zhao, W.; Guo, X.; Zhang, H.; Hu, S.; Huang, Z.; Yin, D. Characteristics of antibiotics and antibiotic resistance genes in Qingcaosha Reservoir in Yangtze River Delta, China. *Environ. Sci. Eur.* **2020**, *32*, 82.

(2) Martinez, J. Environmental pollution by antibiotics and by antibiotic resistance determinants. *Environ. Pollut.* **2009**, *157*, 2893−2902.

(3) Hu, Y.; Zhang, T.; Jiang, L.; Yao, S.; Ye, H.; Lin, K.; Cui, C. Removal of sulfonamide antibiotic resistant bacterial and intracellular antibiotic resistance genes by UVC-activated peroxymonosulfate. *Chem. Eng. J.* **2019**, *368*, 888−895.

(4) He, H.; Zhao, T.; Ma, Q.; Yang, X.; Yue, Q.; Huang, B.; Pan, X. Photoelectrocatalytic coupling system synergistically removal of antibiotics and antibiotic resistant bacteria from aquatic environment. *J. Hazard. Mater.* **2022**, *424*, 127553.

(5) Hou, J.; Chen, J.; Gao, Y.; Xie, L.; Li, L.; Qin, S.; Wang, Q.; Mao, D.; Luo, Y. Simultaneous removal of antibiotics and antibiotic resistance genes from pharmaceutical wastewater using the combinations of up-flow anaerobic sludge bed, anoxic-oxic tank, and advanced oxidation technologies. *Water Res.* **2019**, *159*, 511−520.

(6) Zhou, C.; Wu, J.; Dong, L.; Liu, B.; Xing, D.; Yang, S.; Wu, X.; Wang, Q.; Fan, J.; Feng, L.; Cao, G. Removal of antibiotic resistant bacteria and antibiotic resistance genes in wastewater effluent by UV-activated persulfate. *J. Hazard. Mater.* **2020**, *388*, 122070.

(7) Fernando, K.; Sahu, S.; Liu, Y.; Lewis, W.; Guliants, E.; Jafariyan, A.; Wang, P.; Bunker, C.; Sun, Y. Carbon Quantum Dots and Applications in Photocatalytic Energy Conversion. *ACS Appl. Mater. Interfaces* **2015**, *7*, 8363−8376.

(8) Atchudan, R.; Edison, T. N. J. I.; Perumal, S.; Vinodh, R.; Lee, Y. R. In-situ green synthesis of nitrogen-doped carbon dots for bioimaging and TiO_2 nanoparticles@nitrogen-doped carbon composite for photocatalytic degradation of organic pollutants. *J. Alloys Compd.* **2018**, *766*, 12−24.

(9) Li, C.; Zou, X.; Lin, W.; Mourad, H.; Meng, J.; Liu, Y.; Abdellah, M.; Guo, M.; Zheng, K.; Nordlander, E. Graphitic Carbon Nitride/CdSe Quantum Dot/Iron Carbonyl Cluster Composite for Enhanced Photocatalytic Hydrogen Evolution. *ACS Appl. Nano Mater.* **2021**, *4*, 6280−6289.

(10) Atchudan, R.; Edison, T. N. J. I.; Aseer, K. R.; Perumal, S.; Karthik, N.; Lee, Y. R. Highly fluorescent nitrogen-doped carbon dots derived from Phyllanthus acidus utilized as a fluorescent probe for label-free selective detection of Fe3+ ions, live cell imaging and fluorescent ink. *Biosens. Bioelectron.* **2018**, *99*, 303−311.

(11) Yan, X.; Rahman, S.; Rostami, M.; Tabasi, Z.; Khan, F.; Alodhayb, A.; Zhang, Y. Carbon Quantum Dot-Incorporated Chitosan Hydrogel for Selective Sensing of Hg2+ Ions: Synthesis, Characterization, and Density Functional Theory Calculation. *ACS Omega* **2021**, *6*, 23504−23514.

(12) He, C.; Xu, P.; Zhang, X.; Long, W. The synthetic strategies, photoluminescence mechanisms and promising applications of carbon dots: Current state and future perspective. *Carbon* **2022**, *186*, 91−127.

(13) Manikandan, V.; Lee, N. Green synthesis of carbon quantum dots and their environmental applications. *Environ. Res.* **2022**, *212*, 113283.

(14) Atchudan, R.; Kishore, S. C.; Gangadaran, P.; Edison, T. N. J. I.; Rajendran, R. L.; Alagan, M.; Al-Rashed, S.; Ahn, B.-C.; Lee, Y. R. Tunable fluorescent carbon dots from biowaste as fluorescence ink and imaging human normal and cancer cells. *Environ. Res.* **2022**, *204*, 112365.

(15) Niu, W.; Li, Y.; Zhu, R.; Shan, D.; Fan, Y.; Zhang, X. Ethylenediamine-assisted hydrothermal synthesis of nitrogen-doped carbon quantum dots as fluorescent probes for sensitive biosensing and bioimaging. *Sens. Actuators, B* **2015**, *218*, 229−236.

(16) Qian, Z.; Chai, L.; Tang, C.; Huang, Y.; Chen, J.; Feng, H. A fluorometric assay for acetylcholinesterase activity and inhibitor screening with carbon quantum dots. *Sens. Actuators, B* **2016**, *222*, 879−886.

(17) Sendão, R. M. S.; da Silva, J. C. G. E.; da Silva, L. P. Photocatalytic removal of pharmaceutical water pollutants by TiO_2−Carbon dots nanocomposites: A review. *Chemosphere* **2022**, *301*, 134731.

(18) Wang, K.; Liang, L.; Zheng, Y.; Li, HX.; Niu, XH.; Zhang, DY.; Fan, H. Y. Visible light-driven photocatalytic degradation of organic pollutants via carbon quantum dots/TiO_2. *New J. Chem.* **2021**, *45*, 16168−16178.

(19) Zeng, Y.; Chen, D.; Chen, T.; Cai, M.; Zhang, Q.; Xie, Z.; Li, R.; Xiao, Z.; Liu, G.; Lv, W. Study on heterogeneous photocatalytic ozonation degradation of ciprofloxacin by TiO_2/carbon dots: kinetic, mechanism and pathway investigation. *Chemosphere* **2019**, *227*, 198−206.

(20) Liu, X.; Yang, Y.; Li, H.; Yang, Z.; Fang, Y. Visible light degradation of tetracycline using oxygen-rich titanium dioxide nanosheets decorated by carbon quantum dots. *Chem. Eng. J.* **2021**, *408*, 127259.

(21) Perumal, S.; Edison, T. N. J. I.; Atchudan, R.; Sundramoorthy, A. K.; Lee, Y. R. Green-Routed Carbon Dot-Adorned Silver Nanoparticles for the Catalytic Degradation of Organic Dyes. *Catalysts* **2022**, *12*, 937.

(22) Fu, H.; Wang, B.; Wang, H.; Liu, H.; Xie, H.; Han, L.; Wang, N.; Sun, X.; Feng, Y.; Xue, L. Assessment of livestock manure-derived

hydrochar as cleaner products: Insights into basic properties, nutrient composition, and heavy metal content. *J. Cleaner Prod.* **2022**, *330*, 129820.
(23) Li, D.; Cui, H.; Cheng, Y.; Xue, L.; Wang, B.; He, H.; Hua, Y.; Chu, Q.; Feng, Y.; Yang, L. Chemical aging of hydrochar improves the Cd2+ adsorption capacity from aqueous solution. *Environ. Pollut.* **2021**, *287*, 117562.
(24) Li, D.; Li, H.; Chen, D.; Xue, L.; He, H.; Feng, Y.; Ji, Y.; Yang, L.; Chu, Q. Clay-hydrochar composites mitigated CH4 and N2O emissions from paddy soil: A whole rice growth period investigation. *Sci. Total Environ.* **2021**, *780*, 146532.
(25) Voigt, M.; Bartels, I.; Nickisch-Hartfiel, A.; Jaeger, M. Photoinduced degradation of sulfonamides, kinetic, and structural characterization of transformation products and assessment of environmental toxicity. *Toxicol. Environ. Chem.* **2017**, *99*, 1304−1327.
(26) Ren, S.; Boo, C.; Guo, N.; Wang, S.; Elimelech, M.; Wang, Y. Photocatalytic Reactive Ultrafiltration Membrane for Removal of Antibiotic Resistant Bacteria and Antibiotic Resistance Genes from Wastewater Effluent. *Environ. Sci. Technol.* **2018**, *52*, 8666−8673.
(27) He, X.; Xue, J.; Shi, L.; Kong, Y.; Zhan, Q.; Sun, Y.; Zhang, Q.; Ramakrishna, S.; Dai, Y. Recent antioxidative nanomaterials toward wound dressing and disease treatment via ROS scavenging. *Mater. Today Nano* **2022**, *17*, 100149.
(28) Yang, H.; Wang, P.; Wang, D.; Zhu, Y.; Xie, K.; Zhao, X.; Yang, J.; Wang, X. New Understanding on Photocatalytic Mechanism of Nitrogen-Doped Graphene Quantum Dots-Decorated BiVO4 Nanojunction Photocatalysts. *ACS Omega* **2017**, *2*, 3766−3773.
(29) Li, X.; Ge, F.; Ding, H.; Zhou, X.; Li, X. Nitrogen-doped carbon dots as electron "bridge" in heterostructure of alpha-Fe2O3/NCDs/g-C3N4 for efficient degradation of indole using heterogeneous photo-Fenton. *J. Environ. Chem. Eng.* **2022**, *10*, 106824.
(30) Hsu, C.; Li, C.; Zhang, L.; Lu, S. N-doped carbon dots@layer facilitated heterostructure of TiO_2 polymorphs for efficient photoelectrochemical water oxidation. *J. Taiwan Inst. Chem. Eng.* **2018**, *93*, 388−396.
(31) Dsouza, S.; Buerkle, M.; Brunet, P.; Maddi, C.; Padmanaban, D.; Morelli, A.; Payam, A.; Maguire, P.; Mariotti, D.; Svrcek, V. The importance of surface states in N-doped carbon quantum dots. *Carbon* **2021**, *183*, 1−11.
(32) Wang, Y.; Rinawati, M.; Huang, W.; Cheng, Y.; Lin, P.; Chen, K.; Chang, L.; Ho, K.; Su, W.; Yeh, M. Surface-engineered N-doped carbon nanotubes with B-doped graphene quantum dots: Strategies to develop highly-efficient noble metal-free electrocatalyst for online-monitoring dissolved oxygen biosensor. *Carbon* **2022**, *186*, 406−415.
(33) Muthusankar, G.; Sethupathi, M.; Chen, S.; Devi, R.; Vinoth, R.; Gopu, G.; Anandhan, N.; Sengottuvelan, N. N-doped carbon quantum dots @ hexagonal porous copper oxide decorated multiwall carbon nanotubes: A hybrid composite material for an efficient ultrasensitive determination of caffeic acid. *Composites, Part B* **2019**, *174*, 106973.
(34) Cai, Q.; Hu, J. Effect of UVA/LED/TiO_2 photocatalysis treated sulfamethoxazole and trimethoprim containing wastewater on antibiotic resistance development in sequencing batch reactors. *Water Res.* **2018**, *140*, 251−260.
(35) Wang, K.; Liu, B.; Li, J.; Liu, X.; Zhou, Y.; Zhang, X.; Bi, X.; Jiang, X. In-situ synthesis of TiO_2 nanostructures on Ti foil for enhanced and stable photocatalytic performance. *J. Mater. Sci. Technol.* **2019**, *35*, 615−622.
(36) Sharma, S.; Dutta, V.; Singh, P.; Raizada, P.; Rahmani-Sani, A.; Hosseini-Bandegharaei, A.; Thakur, V. Carbon quantum dot supported semiconductor photocatalysts for efficient degradation of organic pollutants in water: A review. *J. Cleaner Prod.* **2019**, *228*, 755−769.
(37) Atchudan, R.; Edison, T. N. J. I.; Mani, S.; Perumal, S.; Vinodh, R.; Thirunavukkarasu, S.; Lee, Y. R. Facile synthesis of a novel nitrogen-doped carbon dot adorned zinc oxide composite for photodegradation of methylene blue. *Dalton Trans.* **2020**, *49*, 17725−17736.
(38) Luo, Y.; Mao, D.; Rysz, M.; Zhou, D.; Zhang, H.; Xu, L.; Alvarez, P. Trends in Antibiotic Resistance Genes Occurrence in the Haihe River, China. *Environ. Sci. Technol.* **2010**, *44*, 7220−7225.

https://doi.org/10.1021/acsomega.2c05979
ACS Omega 2023, 8, 718−725